iScience

CellPress
OPEN ACCESS

Article

Visualization of erythrocyte stasis in the living human eye in health and disease

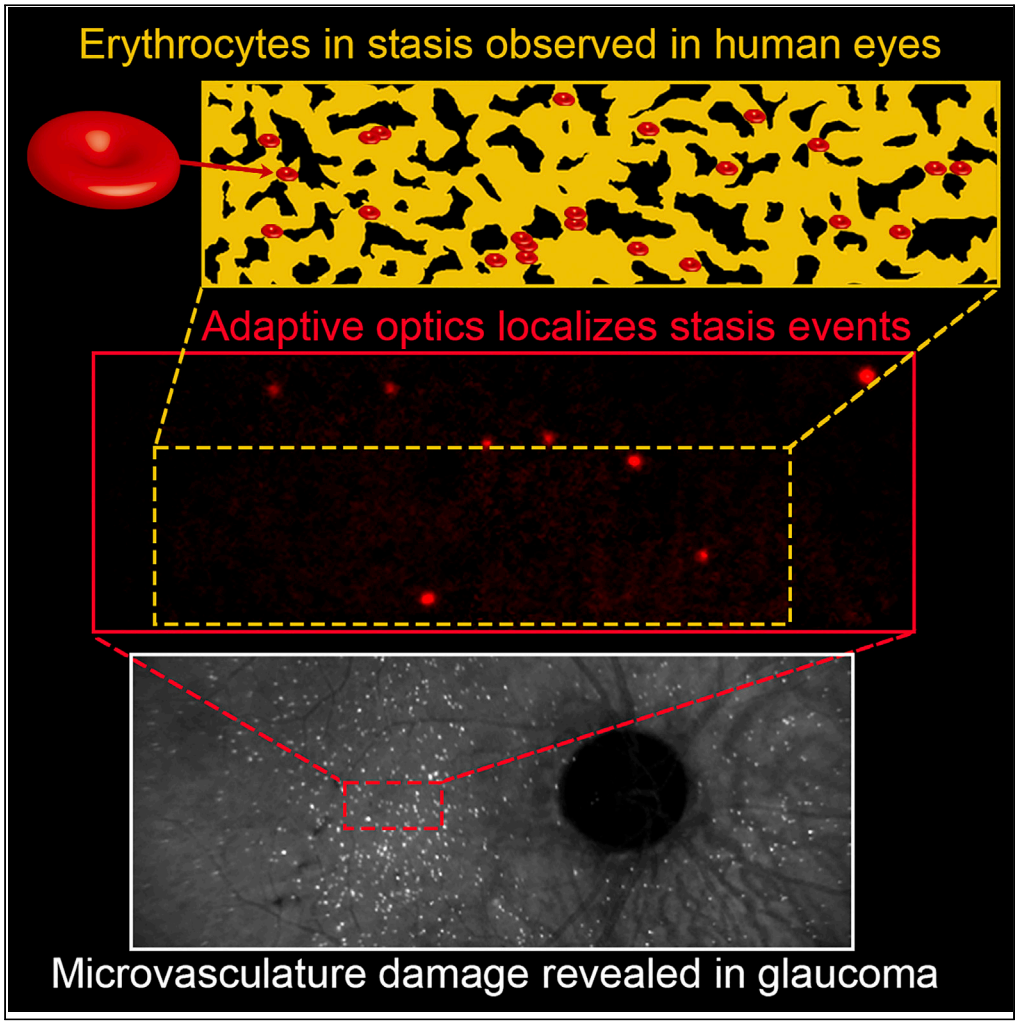

Joanne Li, Dongyi Wang, Jessica Pottenburgh, ..., Yang Tao, Johnny Tam, Osamah J. Saeedi

osaeedi@som.umaryland.edu

Highlights

Erythrocytes in stasis are physiologically robust phenomena in the living human eye

Transient stasis events are a hallmark feature of the choroidal microvasculature

Changes in the distribution of stasis reveals choriocapillaris damage in glaucoma

Adaptive optics can be effectively combined with erythrocyte mediated angiography

Li et al., iScience 26, 105755
January 20, 2023
https://doi.org/10.1016/j.isci.2022.105755

iScience

CellPress
OPEN ACCESS

Article

Visualization of erythrocyte stasis in the living human eye in health and disease

Joanne Li,[1,6] Dongyi Wang,[2,5,6] Jessica Pottenburgh,[3] Andrew J. Bower,[1] Samuel Asanad,[3] Eric W. Lai,[4] Caroline Simon,[4] Lily Im,[3] Laryssa A. Huryn,[1] Yang Tao,[2] Johnny Tam,[1] and Osamah J. Saeedi[3,7,*]

SUMMARY

Blood cells trapped in stasis have been reported within the microcirculation, but their relevance to health and disease has not been established. In this study, we introduce an *in vivo* imaging approach that reveals the presence of a previously-unknown pool of erythrocytes in stasis, located within capillary segments of the CNS, and present in 100% of subjects imaged. These results provide a key insight that blood cells pause as they travel through the choroidal microvasculature, a vascular structure that boasts the highest blood flow of any tissue in the body. Demonstration of clinical utility using deep learning reveals that erythrocyte stasis is altered in glaucoma, indicating the possibility of more widespread changes in choroidal microvascular than previously realized. The ability to monitor the choroidal microvasculature at the single cell level may lead to novel strategies for tracking microvascular health in glaucoma, age-related macular degeneration, and other neurodegenerative diseases.

INTRODUCTION

The choroid is a vascular structure that carries 85% of the blood to the eye and has the highest blood flow per unit weight of any tissue in the body. The choroidal microvasculature, known as the choriocapillaris, supplies blood and nourishment to the outermost layer of the retina, considered to be the most metabolically active tissue in the body, consuming more oxygen per unit weight than the brain.[1] Unlike the retinal vasculature that consists of a network of branched, cylindrical vessels with a relatively colinear arrangement from one branchpoint to the next, the choriocapillaris consists of a planar meshwork of unusually short capillary segments that are fed and drained by orthogonally-connected arterioles and venules from the outer choroid.[2–6] Choroidal vascular dysfunction is implicated in three of the four major causes of blindness worldwide: age related macular degeneration, glaucoma, and diabetic retinopathy.[7–9] Despite its relevance in ocular health and disease, much of our knowledge about the *in vivo* characteristics of blood flow within the choriocapillaris in the living eye is incomplete because it is relatively difficult to image due in part to its thinness and anatomical location behind a pigmented epithelium. The current *in vivo* imaging techniques can provide structural and functional information about the vessels,[4,10,11] but do not reveal how individual blood cells in the living human body travel through the atypical geometry of the choriocapillaris network. Different from most other capillaries, the choriocapillaris lumens are wide (approximately 10 μm in diameter) relative to the size of erythrocytes (approximately 8 μm in diameter). These characteristics distinguish the choriocapillaris from many other microvasculature networks in the body and provide a potentially transformative view of how blood cells travel through distinct capillary networks.

Glaucoma is a neurodegenerative disease in which retinal ganglion cells (RGC) and their axons are injured, leading to neuronal death and vision loss. All of the RGC axons within the eye pass through the optic nerve, the primary site of axonal damage in glaucoma. While elevated intraocular pressure is a primary risk factor for glaucoma, reduced ocular perfusion and impaired autoregulation of blood flow to the eye are also implicated in the disease pathogenesis.[12] In addition, outer retinal circulatory dysfunction has been linked to glaucoma in multiple ways. Recent work has shown localized microvascular dropout or nonperfusion of the choroidal circulation surrounding the optic nerve head,[13,14] even showing that microvascular dropout of the choroid may precede progression of glaucoma.[15,16] But without the ability to visualize blood cells as they flow through the network, it is difficult to fully evaluate the degree to which the choroidal microvasculature is disrupted. These observations motivate our hypothesis that the way in which erythrocytes travel through the choriocapillaris is altered in glaucoma.

[1]National Eye Institute, National Institutes of Health, Bethesda, MD, USA

[2]Bioimaging and Machine Vision Laboratory, Fischell Department of Bioengineering, University of Maryland, College Park, MD, USA

[3]Department of Ophthalmology and Visual Sciences, University of Maryland School of Medicine, Baltimore, MD, USA

[4]University of Maryland School of Medicine, Baltimore, MD, USA

[5]Present address: Biological and Agricultural Engineering Department, University of Arkansas, Fayetteville, AR, USA

[6]These authors contributed equally

[7]Lead contact

*Correspondence: osaeedi@som.umaryland.edu

https://doi.org/10.1016/j.isci.2022.105755

To visualize individual blood cells, we turn to erythrocyte mediated angiography (EMA), in which autologous erythrocytes are labeled with indocyanine green (ICG) dye and re-injected into the subject's veins, resulting in the ability to observe individual erythrocyte movement and dynamics in the non-human primate (NHP) and human eye.[17–19] Importantly, the near-infrared fluorescence wavelength of ICG is able to pass through the pigmented epithelium of the eye so that fluorescent cells are visible in both the retina and choroid, opening up the possibility of visualizing individual blood cells in the choriocapillaris with the proper instrumentation.

Notably, in early EMA reports, there were some erythrocytes noted to be in stasis, or "paused" for a duration of minutes to hours in these angiograms. This is not surprising, given the variation in erythrocyte flux, speed, and even flow direction that has been reported across neighboring capillaries in the eye.[20–23] Erythrocyte stasis could also arise due to vasomotion, possibly from capillary pericytes,[22] and spontaneous erythrocytes in stasis have been previously reported in select capillary segments.[24] Whether the choriocapillaris, with its atypical topology, is a natural site of erythrocyte stasis has not been explored. Although these erythrocytes in stasis can be detected using EMA, to date, these images have been limited in resolution, and the precise localization of these cells in stasis within the retinal and choroidal microvasculature has not been distinguished.

Adaptive optics (AO) retinal imaging techniques have been used to study the various cellular and vascular structures within the retina due to the improved resolution gained by correcting for the optical aberrations in the eyes.[25,26] Among these, AO-enhanced ICG (AO-ICG) imaging has demonstrated the capability to visualize ICG dye in the living human eye,[27,28] and the choriocapillaris structure can be visualized using AO-ICG during the initial passage of dye through the vasculature.[10] In this study, AO-ICG was combined with EMA (AO-EMA) to directly visualize fluorescently-labeled erythrocytes with sufficient lateral and axial resolution to elucidate their locations in the eye relative to the choroidal microvasculature when they are in stasis. This additional information enables a better understanding of the relationship between erythrocyte stasis and vascular function in both healthy and diseased eyes.

RESULTS

Erythrocyte stasis is a robust phenomenon observed in all eyes

Following autologous injection of ICG-labeled erythrocytes, erythrocyte stasis was observed in 100% of the eyes imaged (four NHP and 37 human eyes), consistent with and expanding upon preliminary findings in a smaller cohort of four eyes.[17] Similar to the change in signal described across the early, mid, and late phases of conventional dye-based fundus angiography, the number of autologously-injected fluorescently-labeled erythrocytes visible within the eye also varied in a time-dependent manner after intravenous administration. Erythrocytes in stasis were visible using a scanning laser ophthalmoscope (SLO) after injection, with a gradual decrease in the number of detected cells over the next few hours (Figure 1). We did not observe any examples of long-term residence of fluorescent cells (beyond one day, as confirmed by follow-up imaging). Notably, erythrocyte stasis was observed in every healthy eye imaged (n = 10), suggesting that these cells in stasis occur under normal physiological conditions.

Erythrocytes in stasis observed within the foveal avascular zone

Erythrocyte stasis was observed across the posterior pole of the eye, including in the foveal avascular zone (FAZ), which does not contain retinal vessels and was mapped out using optical coherence tomography angiography (OCTA). Across eight imaging sessions performed on two NHPs (four imaging sessions per NHP), erythrocytes in stasis were observed within the FAZ of at least one eye of each NHP per imaging session (Figure 2), with a mean $\pm$ SD number of cells in stasis in the FAZ across all imaging sessions of 1.4 $\pm$ 1.1 (ranging from 0 to 4). Since erythrocyte stasis was frequently observed in the FAZ across these imaging sessions, the NHP data indicates a high likelihood that there are erythrocytes in stasis outside of the retinal vasculature, which would suggest the presence of erythrocyte stasis within the choroidal microvasculature.

Building upon these observations that there were erythrocyte stasis present within the FAZ of NHP eyes (Figure 2), further work in a cohort of human eyes showed these findings were reproducible (Table S1). Erythrocyte stasis within the FAZ was observed in 28 out of 31 eyes (90.3%, 9 out of 9 glaucoma eyes, 15 out of 16 glaucoma suspect eyes, and 4 out of 6 control eyes). There were no statistically significant differences for the total number of cells in stasis within the FAZ across the patient cohorts based on generalized estimating equation analysis ($p = 0.44$). There was an average of 4.7 $\pm$ 4.7 erythrocytes in stasis in the FAZ

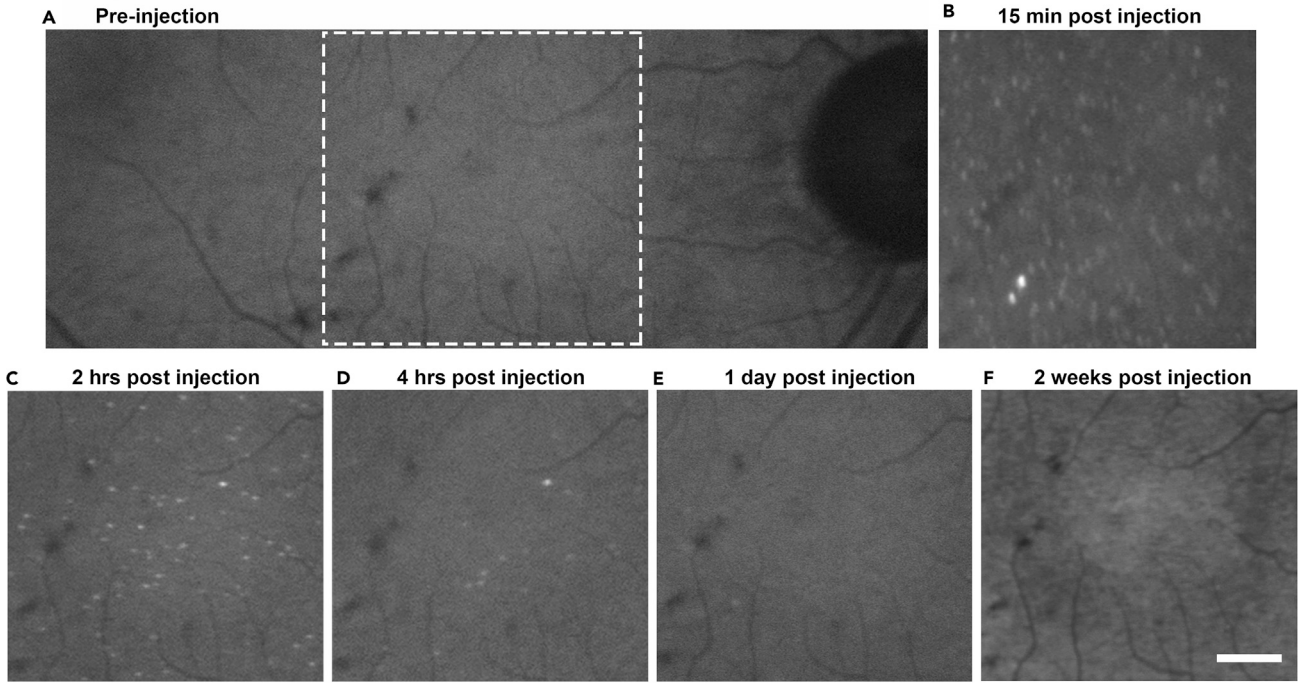

Figure 1. Time course of erythrocytes in stasis following erythrocyte-mediated angiography (EMA) injection

Heidelberg scanning laser ophthalmoscopy (SLO) images of the retina at time points (A) before and (B–F) after the EMA procedure.

(A) Pre-injection image shows that no ICG signal was observed in the eye (the faint, background infrared autofluorescence signal can be seen).

(B–F) SLO image acquired after the EMA procedure (in dashed box in [A]) shows the locations of erythrocytes in stasis changing over time. (B) 15 min after the injection, many stasis events with varying levels of brightness can be seen. (C) After 2 h, stasis events were observed in various locations across the retina but with slightly less cells than earlier. There was a decrease in the number of stasis events (D) after 4 h, with a further decrease observed (E) one day afterward. (F) No ICG signal was observed in the eye two weeks post procedure. Scale bar: 200 μm.

overall (5.0 ± 2.8 for glaucoma eyes, 3.9 ± 3.2 for glaucoma suspect eyes, and 6.5 ± 9.0 for control eyes; mean ± SD). Since the FAZ is an area devoid of retinal vessels (but still contains choroidal vessels), these results suggest that there are at least some erythrocytes in stasis within the choroidal vasculature in the large majority of eyes, opening up the possibility for visualizing fluorescently-labeled individual blood cells in the choriocapillaris in the living human eye.

Layer-specific localization using AO-EMA

The time course of erythrocyte stasis provided an opportunity to image them using AO-SLO over a time period of several hours. Erythrocytes in stasis were successfully imaged using the combined AO-EMA approach (Figures 3A and 3B). Due to the sequential imaging (alternating between SLO and AO), more stasis was observed in the SLO image acquired at an earlier time point (Figure 3A) compared to the subsequently-acquired AO image (Figure 3B), consistent with the gradual reduction in stasis over the first few hours after injection (Figure 1). However, the same overall spatial pattern of these cells could be seen in both SLO and AO images, confirming that a subset of cells were successfully imaged across both the SLO and AO images, which could be used for further analysis. As expected, AO images had higher lateral and axial resolution compared to the SLO images due to the ~4-5X larger imaging beam diameter and the correction of both lower and higher order optical aberrations,[29] which facilitated the layer-specific localization of these cells in stasis using AO-EMA.

We examined whether the stasis was occurring in the retinal vasculature or the choroidal vasculature by sequentially acquiring AO images with the focal planes set in both the retina and choroid. To compare images of the same cell acquired at two different focal planes, full width at half maximum (FWHM) measurements of the ICG signal profile was calculated. This measurement calculates the width on the profile curve between two points where the signal intensity is half of the maximum intensity (Figure S1). When imaged

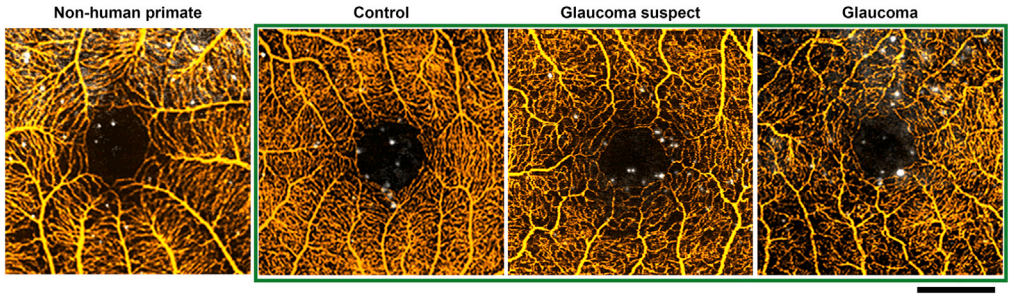

Figure 2. Erythrocytes in stasis were observed within the foveal avascular zone (FAZ) in majority of the eyes

Erythrocyte mediated angiography (EMA) was performed in which indocyanine green (ICG)-loaded erythrocytes are autologously injected and imaged. Optical coherence tomography angiography (OCTA) images demarcate the location of the FAZ (central black area), a region that lacks retinal vasculature. Images of fluorescently-labeled erythrocytes (white circular dots), captured using SLO and overlaid on the OCTA images, reveal the presence of erythrocytes in stasis within the FAZ. Similar results were observed in both non-human primate (NHP) eyes and human eyes (enclosed in green box). In human eyes, erythrocytes in stasis were present in control, glaucoma suspect, and glaucoma eyes, establishing that stasis is a robust physiological phenomenon. Scale bar: 1 mm.

with AO, a technique that corrects for optical aberrations, these measurements indicate how well an object is in focus – an out-of-focus cell will result in larger FWHM value compared to the value of a cell that is in focus. Across two eyes of two subjects, 19 out of 19 (100%) of the cells that were sequentially imaged using AO-EMA were located in the choroidal vasculature, both for cells that were within the FAZ as well as for cells that were outside of the FAZ.

To further characterize the layer-specific localization of each of the erythrocytes in stasis, in a follow up imaging session, we obtained a series of sequentially-acquired AO images with fine sampling (approximately 35 μm step size) of the focal plane across the layers within the eye (Figures 3C and 3D). These image sequences revealed that 100% of the cells imaged using this fine-sampling approach (n = 7 cells) were increasingly blurrier (out of focus) at focal planes further away from the choriocapillaris layer. Combined, our data across three AO-EMA procedures performed in two subjects (n = 26 distinct cells) indicate that erythrocyte stasis is predominantly occurring in the choriocapillaris, as opposed to the retinal vasculature.

Correlative multimodal imaging of erythrocyte stasis reveals localization to the choroidal microvasculature

By correlating multimodal AO images with SLO images acquired over multiple time points and across multiple visits, the locations of a complete set of erythrocytes in stasis relative to the choroidal microvasculature were tracked. High resolution images of the parafoveal capillaries surrounding the FAZ confirmed the presence of numerous erythrocytes in stasis that did not co-localize to the retinal vasculature, even in areas outside of the FAZ (Figures 4A and 4B), further corroborating our claim that the observed stasis is occurring outside of the retinal vasculature, and consistent with our FWHM data that showed that these erythrocytes in stasis were within the choriocapillaris layer. Here, we determined the *x-y* location of cells in stasis relative to the choroidal microvasculature by first mapping out the choriocapillaris using AO-ICG angiography,[10] and then by spatially registering this choriocapillaris map with images of erythrocytes in stasis acquired by both AO-SLO and SLO from multiple EMA procedures across three years (Figures 4C and S2). Strikingly, across a total of 66 erythrocytes in stasis identified within an ~860 μm × 250 μm area using this correlative multimodal imaging approach, every single cell in stasis identified was located within a choriocapillaris vessel segment. Since the choriocapillaris is a thin anatomical layer, it was possible that there could have been erythrocytes in stasis in deeper choroidal layers. However, if this were the case, then we would expect to see some cells in stasis occurring outside of the choriocapillaris lumen areas, which we were not able to identify in this cohort. In addition, the FWHM measurements would have indicated that at least some of these cells were located in deeper choroidal layers. The likelihood that all of these cells in stasis from different timepoints and different visits were all located within the choriocapillaris segments, as opposed to within the flow voids, was statistically significant ($p < 0.001$, binomial test). Taken together with our FWHM measurement data, these results establish that erythrocyte stasis is occurring within the choriocapillaris vessels.

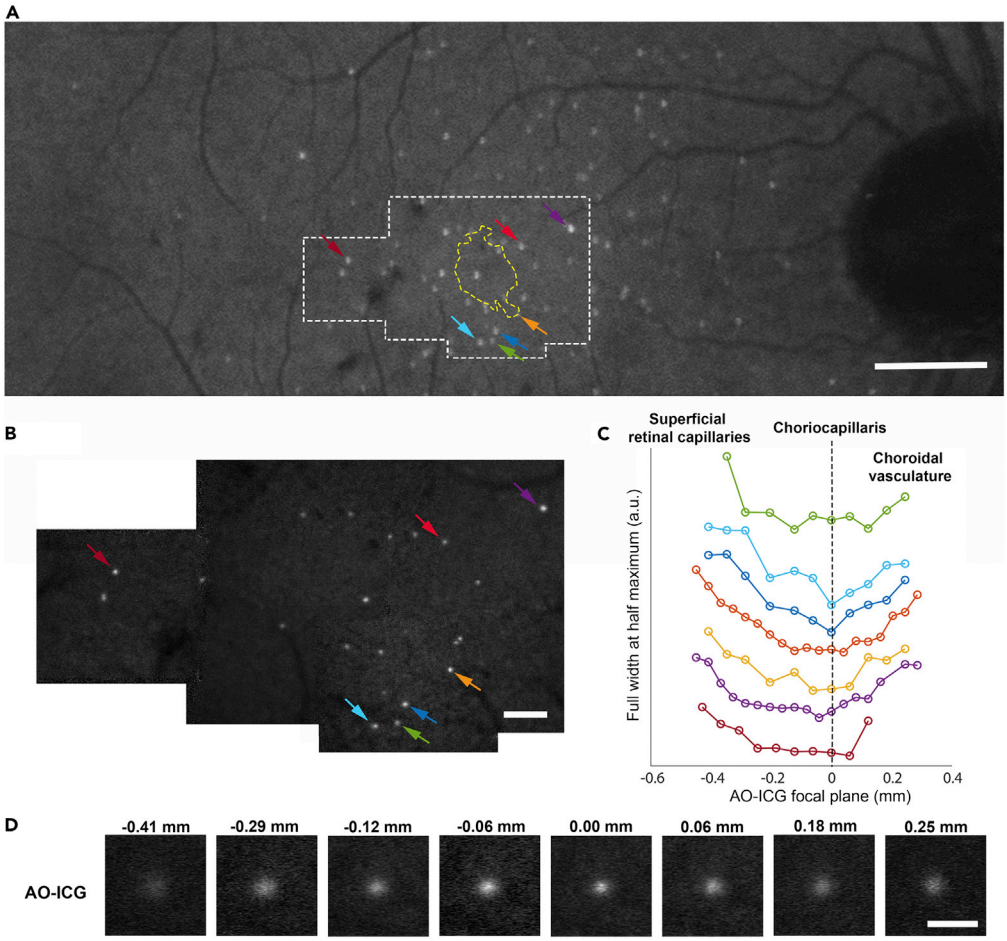

Figure 3. Erythrocytes in stasis were located within the choriocapillaris layer of the human eye

(A) SLO image showing the distribution of erythrocytes in stasis across the eye.

(B) Higher resolution AO-ICG images of the white dashed region in (A) showing a subset of the erythrocytes in stasis, acquired 30 to 40 min after the image in (A). here, the focal plane is set at the choriocapillaris layer. The fluorescently-labeled blood cells all appear to be in focus across the AO images (yellow dashed line: foveal avascular zone [FAZ] boundary).

(C) Full width at half maximum (FWHM) measurements of seven of the cells imaged using AO-ICG across different focal planes confirm that the cells are in best focus near the choriocapillaris focal plane. Each color in (C) corresponds to one cell in (A and B) identified by the color matched arrows. These plots also confirmed that erythrocytes in stasis were not located in the retinal vasculature. Plots from individual cells are vertically displaced for visualization purposes.

(D) A series of AO-ICG images of an erythrocyte in stasis (dark blue arrow in [A and B]) across different focal planes, showing that the cell is in best focus when the focal plane is set near the choriocapillaris (0.00 mm). Scale bars: (A) 1 mm; (B) 100 μm; (D) 70 μm.

Distribution of erythrocyte stasis across the choroidal microvasculature is altered in glaucoma

To further characterize the distribution of erythrocyte stasis in health and disease, EMA was used to evaluate the choroidal microvasculature in glaucoma (including both glaucoma and glaucoma suspect eyes; Table S1). A total of 5,823 erythrocytes in stasis were objectively identified in a subset of 21 eyes (15 glaucoma, 6 controls) from 16 subjects using an automated cell detection deep learning algorithm (Figure S3 and Table S2). Stasis in the macula and peripapillary regions were analyzed and compared (Figure 5). Interestingly, in glaucoma eyes, there were significantly less erythrocytes in stasis in the peripapillary retina as compared to the macula (102.9 $\pm$ 46.1 in the peripapillary retina and 236.5 $\pm$ 89.7 in the macula, $p < 0.001$) (Figure 5C). This phenomenon was not observed in the control subjects (122.9 $\pm$ 47.3 in the peripapillary retina and 146.1 $\pm$ 83.7 in the macula, $p = 0.335$). To further characterize the relative distribution of cells in

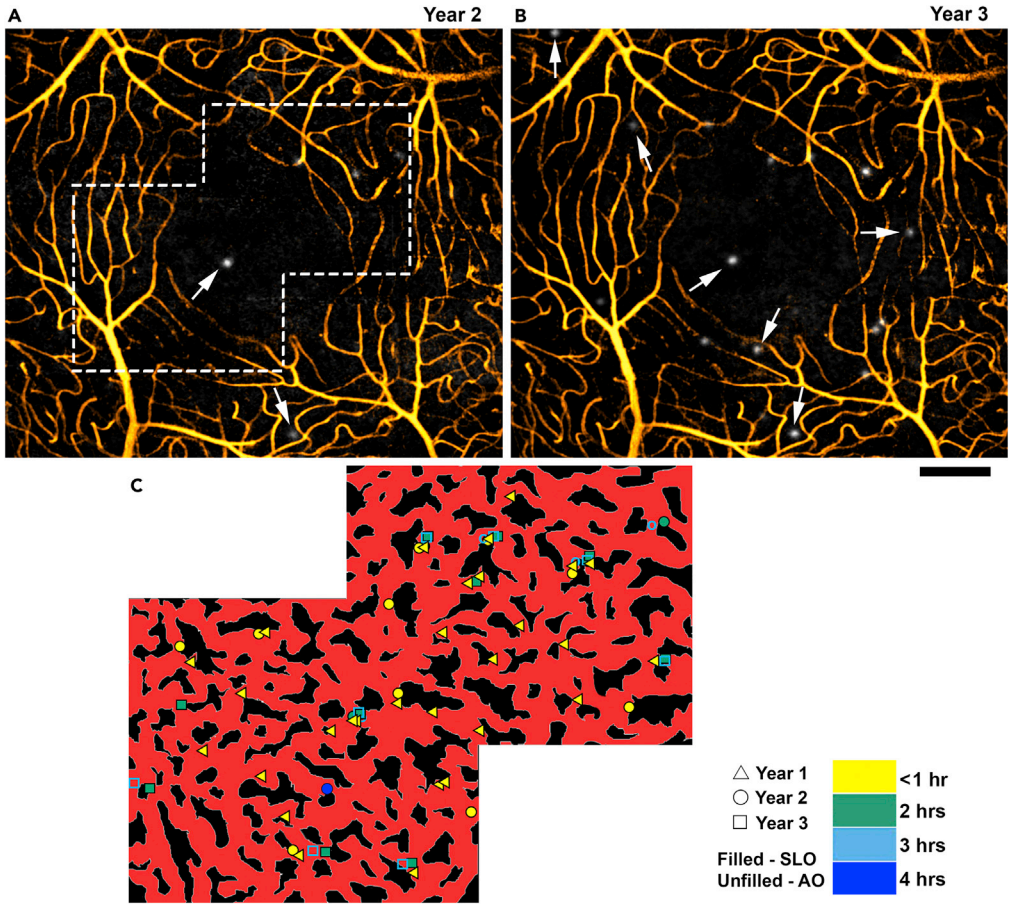

Figure 4. Erythrocyte stasis occurred within the short vessel segments of the choroidal microvasculature

Only standard EMA was performed in year 1, and both standard EMA and AO-EMA were performed in years 2 and 3. (A and B) Higher resolution AO images of erythrocyte in stasis (white circular dots imaged using AO-ICG; [A]: year 2, [B]: year 3) co-registered to AO images of the inner retinal microvasculature (yellow, imaged using AO non-confocal split detection). (C) In this segmentation map of the choriocapillaris (Figure S2), the images of the retinal vessels were acquired at a focal plane that was anterior to the erythrocytes in stasis. Erythrocyte stasis marked from multiple timepoints associated with three separate EMA procedures across three years. Cells recorded from different years and procedures are categorized by different markers (filled markers: imaged using SLO; unfilled markers: imaged using AO). The colormap indicates the time points at which these cells in stasis were captured by imaging. All of the cells in stasis that could be identified within this region were located within the choriocapillaris vessel segments. Scale bar: 200 μm.

stasis, we introduced a simple quantitative metric calculated based on the ratio between the peripapillary retina and macula (PMR). As expected, the PMR was significantly skewed in glaucoma when compared to control eyes (0.43 ± 0.14 in glaucoma; 0.93 ± 0.27 in control eyes; $p < 0.001$, generalized estimating equation) (Figure 5D). These findings are suggestive of local functional or structural changes, in the choriocapillaris network near the optic nerve head in glaucoma. There were no observed differences in heart rate, respiratory rate, blood pressure, or temperature either due to the EMA procedure or when comparing patients with glaucoma to healthy subjects.

DISCUSSION

The current understanding of the choriocapillaris in health and disease has been largely based on structural imaging or *ex vivo* histological studies in which flow patterns are often modeled as discrete "functional lobules", clusters of neighboring choriocapillaris vessel segments organized around a central precapillary arteriole.[30–33] In this paper, we introduce a natural combination of two complementary techniques (AO-EMA)[10,17,18,28] which revealed the presence of a previously-undiscovered population of erythrocytes in stasis that are concealed within the choroidal microvasculature.

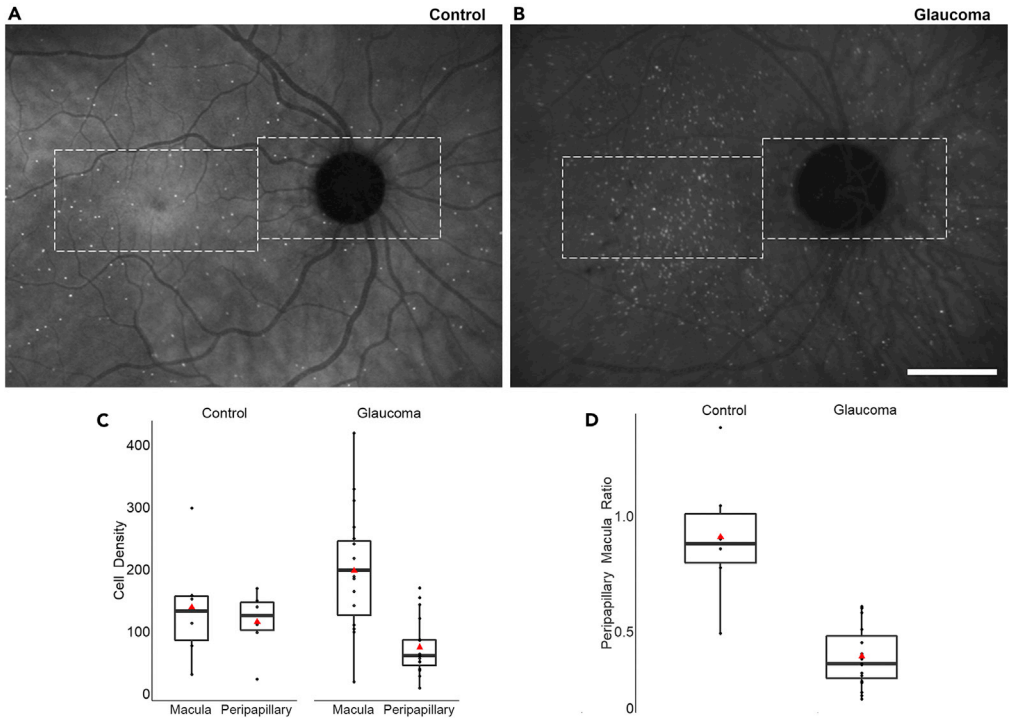

Figure 5. EMA was performed on human using ICG-loaded erythrocytes, allowing for the characterization of the retinal distribution of cells in stasis in both healthy and diseased eyes

(A and B) Averaged, wide field-of-view SLO images from control and glaucoma subjects show the distribution of stationary cells in the macula and peripapillary regions (white dashed area).

(C) Boxplot showing the absolute number of erythrocytes in stasis density (cell density) in the macula and peripapillary regions were similar for control subjects, while in glaucoma subjects, the macula cell densities were higher than peripapillary cell densities (center line: median, red triangle: mean, box limits: upper/lower quartiles, whiskers: 1.5x interquartile range, black dots: individual data points).

(D) The decreased peripapillary to macula ratio (PMR) value for glaucoma subjects compared to controls indicates less cells in stasis in glaucomatous eyes around the optic nerve, a region known to be affected by glaucoma pathogenesis. Scale bar: 2 mm.

The observations of erythrocytes in stasis observed within the FAZ (Figure 2) and in areas that are between retinal capillaries (Figures 4A and 4B), combined with the localization of these cells in stasis to the choriocapillaris lumen in both the axial (Figure 3C) and lateral (Figure 4D) dimensions suggest that the erythrocyte stasis in the posterior pole primarily occurs within the choroidal microcirculation. As only *de novo* stasis can be revealed using EMA, it is likely that there are additional erythrocytes in stasis at any given time which are undetected. For a typical EMA injection, less than 0.05% of the total blood volume contains fluorescently-labeled erythrocytes and so it is likely that only a fraction of the cells in stasis are captured. It is also possible that the number of cells in stasis is related to factors specific to each individual, including choriocapillaris architecture and the effective blood volume. The temporal dynamics (Figure 1) suggest that these cells in stasis spontaneously occur inside the choriocapillaris and can remain stable for minutes to hours. This turnover of erythrocytes in stasis would allow the cells to return to the circulation at some point without affecting the overall blood flow within the specific tissues.

A computational fluid dynamics simulation[34,35] of individual red blood cells flowing through a retinal capillary network showed the presence of erythrocytes in stasis, which seemed to occur most frequently in short vessel segments that appeared to bridge two thoroughfare channels[36] (in this simulation, the capillary diameter was assumed to be 10 μm, similar in size to the choriocapillaris vessel lumen). Our findings are consistent with this simulation, which support our hypothesis that erythrocyte stasis is a hallmark of the choroidal microvasculature largely established by the structure of the capillary bed itself rather than by the rheology of individual erythrocytes. In particular, it has been postulated that erythrocyte stiffness, which can increase due to aging, hypertension, or diabetes,[37–39] can influence capillary flow at the single cell

level. However, studies evaluating erythrocyte deformability as measured by filtration rates have shown that erythrocyte ghosts have lower deformability indices (i.e. are more efficient at flowing through a filter) than native erythrocytes.[37,40] The ICG-loaded erythrocytes used for EMA[17] are similar to ghost erythrocytes which have been extensively explored as carriers for biopharmaceuticals.[41] These previous findings imply that ICG-loaded erythrocytes are less likely than native erythrocytes to spontaneously enter into stasis.

From a structural perspective, considering the higher than typical number of short, interconnecting vessel segments that are characteristic of the choriocapillaris, it is not surprising that erythrocytes in stasis are more abundant in the choriocapillaris when compared to the retinal capillaries, which contain a smaller number of short, interconnecting vessel segments[22,23] and would therefore be expected to have fewer cells in stasis. It is also likely that any erythrocytes in stasis occurring within the retinal vasculature would remain in stasis for a shorter amount of time than those occurring within the choriocapillaris due to the difference in vascular structure. It is also important to note that while in the smallest retinal capillaries, which feature single-file flow of individual blood cells, an erythrocyte in stasis could temporarily occlude blood flow; in contrast, the larger lumen diameter of the choriocapillaris would in theory permit other erythrocytes to flow past a single erythrocyte in stasis.

After establishing that erythrocyte stasis is a physiologically robust phenomenon observed in all eyes, we showed that the distribution of erythrocyte in stasis is significantly changed in glaucoma when compared to healthy eyes. Since the majority of the glaucoma cohort included glaucoma suspects, it's possible that these disruptions to the choroidal microvasculature may represent an early indicator of disease. We found a statistically significant difference when taking the ratio between the number of cells in stasis in the peripapillary and macular regions, which may help to account for inter-subject variability observed in the absolute number of cells in stasis observed. Our observations build upon previous studies that have reported peripapillary atrophy of the retina and choroid associated with both the development and progression of glaucoma.[42] A clinicopathologic correlation of enucleated eyes suggested that the peripapillary choriocapillaris may be responsible for peripapillary atrophy associated with glaucomatous degeneration.[43] More recently, swept source OCTA imaging has shown choroidal microvascular dropout in areas of peripapillary atrophy that precedes glaucomatous structural damage, specifically thinning of the retinal nerve fiber layer.[13–16] These previous studies are consistent with the notion that glaucoma is more than a disease of the inner retina, and that the choroidal and choriocapillaris circulation may be linked to the optic nerve circulation. Taking these studies into consideration, it is possible that the relative reduction in stasis events observed in the peripapillary area could be the result of dropout of short choriocapillaris segments in which stasis events would have been expected to occur.

Up until now, choroidal flow disruptions extending beyond the immediate vicinity of the optic nerve head has only been speculated and regional differences in choriocapillaris function unexplored. Our work establishes that the peripapillary choriocapillaris may be more affected than the macular choriocapillaris, which is not surprising, considering that the choriocapillaris shares a common blood supply with the lamina cribrosa (short posterior ciliary artery), and may even contribute to the nourishment of the prelaminar optic nerve head. Additionally, the lack of an autoregulatory response to elevated intraocular pressure[44] may also make the peripapillary region more susceptible to damage arising from functional changes of the choriocapillaris. Such functional changes in the pattern of blood flow itself could also result in further changes in the pattern of stasis observed in glaucomatous eyes. Finally, it is also intriguing to consider that the choriocapillaris shares a common blood supply with the optic nerve head, providing a possible link between early choriocapillaris dysfunction and nerve damage associated with glaucomatous optic neuropathy. However, future studies are needed to elucidate potential relationships between choriocapillaris structure, changes in blood flow pattern, and glaucomatous optical neuropathy.

The relative reduction in the number of stasis observed around the optic nerve is consistent with changes in choriocapillaris in this area. For example, this could result from having fewer vessels or fewer branch points in the choriocapillaris network, as illustrated by an example of a lack of erythrocyte stasis in one subject with presumed toxoplasma retinochoroiditis, a disease which permanently affects choriocapillaris vasculature (Figure S4). In this subject, there was a relative lack of erythrocyte stasis within the lesion when compared to the areas outside of the lesion. OCTA also showed that the overlying retinal vessels were intact, supporting our interpretation that the lack of stasis was reflective of choroidal vascular defects as opposed to retinal vascular defects. This illustrative example supports our notion that damage to

the choriocapillaris vascular architecture may result in reduced erythrocyte stasis. More broadly, the propensity for these cells in stasis to occur in short vessel segments (Figure 4C) illustrates how EMA may be useful as a tool for monitoring choriocapillaris functions in different areas of the eye that may be locally affected by disease.

This study establishes that there is a physiologically robust phenomenon of erythrocytes in stasis within the choriocapillaris, which occasionally can remain in stasis for minutes to hours despite the relatively high volume of blood that flows through this capillary bed. Although this study represents, to our knowledge, the largest cohort to date of *in vivo* EMA, more subjects across a wider age range and longitudinal studies are needed in the future to gain better understanding of these transient stasis events in the choroidal microcirculation. We expect AO-EMA to reveal exciting new possibilities for visualizing the way individual blood cells flow through the choriocapillaris network which cannot currently be performed by any other means, *in vivo* or *ex vivo*. Demonstration of potential clinical utility in glaucoma using deep learning suggests that tracking stasis events could be useful as a quantitative metric for identifying possible local changes to the choroidal microvasculature. Aside from glaucoma, choriocapillaris damage has also been implicated in other eye diseases, including age-related macular degeneration and diabetic retinopathy.[3,45,46] This is consistent with prior reports of decreased erythrocyte stasis in areas of the retina affected by macular degeneration or retinal vein occlusion.[17] Dropout of key capillary segments as well as changes in microvascular blood flow in these diseases could also manifest with changes in the distribution of erythrocyte stasis. These initial insights into how individual blood cells travel through the choroidal microcirculation in health and disease may lead to novel strategies for early detection and tracking of microvascular damage. Ultimately, the combination of AO with EMA introduces a tool for monitoring the microvascular health in other neurodegenerative diseases such as Parkinson and Alzheimer diseases.[47]

Limitations of the study

In this study, AO imaging was performed at a time point of at least 1 h post EMA injection. Earlier time points were not possible due to the time required to travel between research sites. In future studies, recruitment of additional subjects across different age groups may provide further insights into the role of aging on stasis events. Finally, evaluation of EMA in other diseases could further elucidate the relationship between erythrocytes in stasis and the overall health of neurovascular tissues.

STAR★METHODS

Detailed methods are provided in the online version of this paper and include the following:

- KEY RESOURCES TABLE
- RESOURCE AVAILABILITY
  - Lead contact
  - Materials availability
  - Data and code availability
- EXPERIMENTAL MODEL AND SUBJECT DETAILS
  - Non-human primates
  - Human subjects
  - EMA preparation
- METHOD DETAILS
  - NHP imaging
  - Standard EMA in human
  - AO-EMA
  - Data processing and analysis
- QUANTIFICATION AND STATISTICAL ANALYSIS

SUPPLEMENTAL INFORMATION

Supplemental information can be found online at https://doi.org/10.1016/j.isci.2022.105755.

ACKNOWLEDGMENT

We thank D. Cunningham, M Arango, G Babilonia-Ayukawa, B. Gildersleeve, D. Claus, S. Suy, and C. Appleman for assistance with study procedures in the NIH NEI Eye Clinic. We also thank T. Liu for helpful

technical discussions about the AO data. This study was supported in part by the NIH NEI Intramural Research Program, the University of Maryland Baltimore, Institute for Clinical & Translational Research (ICTR) and the National Center for Advancing Translational Sciences (NCATS) Clinical Translational Science Award (CTSA) grant number 1UL1TR003098. This study was also supported by an NIH/NEI grant R01EY031731. EW Lai and C. Simon were supported by grants from the Program for Research Initiated by Students and Mentors (PRISM) at the University of Maryland, Baltimore.

AUTHOR CONTRIBUTIONS

Concept and study design: JT and OJS, Acquisition and analysis of data: JL, DW, JP, AJB, SA, EWL, CS, LI, LAH, JT, OJS, Interpretation of data: JL, DW, JP, AJB, SA, LAH, YT, JT, OJS, Patient referral: OJS, Manuscript drafting: JL, DW, JP, JT, OJS, Critical revision of manuscript: all.

DECLARATION OF INTERESTS

OJ Saeedi received financial and nonfinancial support from Heidelberg Engineering. The other authors declare no competing interests.

Received: April 14, 2022
Revised: August 25, 2022
Accepted: December 5, 2022
Published: January 20, 2023

REFERENCES

1. Wangsa-Wirawan, N.D., and Linsenmeier, R.A. (2003). Retinal oxygen: fundamental and clinical aspects. Arch. Ophthalmol. *121*, 547–557. https://doi.org/10.1001/archopht.121.4.547.

2. Fryczkowski, A.W., and Sherman, M.D. (1988). Scanning electron microscopy of human ocular vascular casts: the submacular choriocapillaris. Acta Anat. *132*, 265–269. https://doi.org/10.1159/000146586.

3. Lejoyeux, R., Benillouche, J., Ong, J., Errera, M.-H., Rossi, E.A., Singh, S.R., Dansingani, K.K., da Silva, S., Sinha, D., Sahel, J.-A., et al. (2022). Choriocapillaris: fundamentals and advancements. Prog. Retin. Eye Res. *87*, 100997. https://doi.org/10.1016/j.preteyeres.2021.100997.

4. Zouache, M.A., Eames, I., Klettner, C.A., and Luthert, P.J. (2016). Form, shape and function: segmented blood flow in the choriocapillaris. Sci. Rep. *6*, 35754. https://doi.org/10.1038/srep35754.

5. Olver, J.M. (1990). Functional anatomy of the choroidal circulation: methyl methacrylate casting of human choroid. Eye *4*, 262–272. https://doi.org/10.1038/eye.1990.38.

6. Yoneya, S., Tso, M.O., and Shimizu, K. (1983). Patterns of the choriocapillaris. Int. Ophthalmol. *6*, 95–99. https://doi.org/10.1007/BF00127637.

7. Jonas, J.B., Forster, T.M., Steinmetz, P., Schlichtenbrede, F.C., and Harder, B.C. (2014). Choroidal thickness in age-related macular degeneration. Retina *34*, 1149–1155. https://doi.org/10.1097/iae.0000000000000035.

8. Pemp, B., and Schmetterer, L. (2008). Ocular blood flow in diabetes and age-related macular degeneration. Can. J. Ophthalmol. *43*, 295–301. https://doi.org/10.3129/i08-049.

9. Dimitrova, G., Kato, S., Tamaki, Y., Yamashita, H., Nagahara, M., Sakurai, M., Kitano, S., and Fukushima, H. (2001). Choroidal circulation in diabetic patients. Eye *15*, 602–607. https://doi.org/10.1038/eye.2001.193.

10. Jung, H., Liu, T., Liu, J., Huryn, L.A., and Tam, J. (2018). Combining multimodal adaptive optics imaging and angiography improves visualization of human eyes with cellular-level resolution. Commun. Biol. *1*, 189. https://doi.org/10.1038/s42003-018-0190-8.

11. Migacz, J.V., Gorczynska, I., Azimipour, M., Jonnal, R., Zawadzki, R.J., and Werner, J.S. (2019). Megahertz-rate optical coherence tomography angiography improves the contrast of the choriocapillaris and choroid in human retinal imaging. Biomed. Opt. Express *10*, 50–65. https://doi.org/10.1364/boe.10.000050.

12. Jones, A., Kaplowitz, K., and Saeedi, O. (2014). Autoregulation of optic nerve head blood flow and its role in open-angle glaucoma. Expert Rev. Ophthalmol. *9*, 487–501. https://doi.org/10.1586/17469899.2014.975796.

13. Jo, Y.H., Shin, J.W., Song, M.K., Won, H.J., and Kook, M.S. (2020). Choroidal microvasculature dropout is associated with generalized choroidal vessel loss within the β-parapapillary atrophy in glaucoma. Am. J. Ophthalmol. *215*, 37–48. https://doi.org/10.1016/j.ajo.2020.03.009.

14. Park, H.Y.L., Kim, J.W., and Park, C.K. (2018). Choroidal microvasculature dropout is associated with progressive retinal nerve fiber layer thinning in glaucoma with disc hemorrhage. Ophthalmology *125*, 1003–1013. https://doi.org/10.1016/j.ophtha.2018.01.016.

15. Kim, J.-A., Lee, E.J., and Kim, T.-W. (2019). Evaluation of parapapillary choroidal microvasculature dropout and progressive retinal nerve fiber layer thinning in patients with glaucoma. JAMA Ophthalmol. *137*, 810–816. https://doi.org/10.1001/jamaophthalmol.2019.1212.

16. Park, H.Y.-L., Shin, D.Y., Jeon, S.J., and Park, C.K. (2019). Association between parapapillary choroidal vessel density measured with optical coherence tomography angiography and future visual field progression in patients with glaucoma. JAMA Ophthalmol. *137*, 681–688. https://doi.org/10.1001/jamaophthalmol.2019.0422.

17. Flower, R.W., and Kling, R. (2017). Observation and characterization of microvascular vasomotion using erythrocyte mediated ICG angiography (EM-ICG-A). Microvasc. Res. *113*, 78–87. https://doi.org/10.1016/j.mvr.2017.02.006.

18. Flower, R., Peiretti, E., Magnani, M., Rossi, L., Serafini, S., Gryczynski, Z., and Gryczynski, I. (2008). Observation of erythrocyte dynamics in the retinal capillaries and choriocapillaris using icg-loaded erythrocyte ghost cells. Invest. Ophthalmol. Vis. Sci. *49*, 5510–5516. https://doi.org/10.1167/iovs.07-1504.

19. Asanad, S., Park, A., Pottenburgh, J., Siddiqui, A., Mayo, L., and Saeedi, O.J. (2021). Erythrocyte-mediated angiography: quantifying absolute episcleral blood flow in humans. Ophthalmology *128*, 799–801. https://doi.org/10.1016/j.ophtha.2020.09.010.

20. Bedggood, P., and Metha, A. (2019). Imaging relative stasis of the blood column in human retinal capillaries. Biomed. Opt. Express *10*,

6009–6028. https://doi.org/10.1364/BOE.10.006009.

21. Gu, B., Wang, X., Twa, M.D., Tam, J., Girkin, C.A., and Zhang, Y. (2018). Noninvasive *in vivo* characterization of erythrocyte motion in human retinal capillaries using high-speed adaptive optics near-confocal imaging. Biomed. Opt. Express *9*, 3653–3677. https://doi.org/10.1364/BOE.9.003653.

22. Schallek, J., Geng, Y., Nguyen, H., and Williams, D.R. (2013). Morphology and topography of retinal pericytes in the living mouse retina using in vivo adaptive optics imaging and *ex vivo* characterization. Invest. Ophthalmol. Vis. Sci. *54*, 8237–8250. https://doi.org/10.1167/iovs.13-12581.

23. Tam, J., Tiruveedhula, P., and Roorda, A. (2011). Characterization of single-file flow through human retinal parafoveal capillaries using an adaptive optics scanning laser ophthalmoscope. Biomed. Opt. Express *2*, 781–793. https://doi.org/10.1364/BOE.2.000781.

24. Guevara-Torres, A., Joseph, A., and Schallek, J.B. (2016). Label free measurement of retinal blood cell flux, velocity, hematocrit and capillary width in the living mouse eye. Biomed. Opt. Express *7*, 4228–4249. https://doi.org/10.1364/BOE.7.004228.

25. Liang, J., Williams, D.R., and Miller, D.T. (1997). Supernormal vision and high-resolution retinal imaging through adaptive optics. J. Opt. Soc. Am. Opt. Image Sci. Vis. *14*, 2884–2892. https://doi.org/10.1364/JOSAA.14.002884.

26. Burns, S.A., Elsner, A.E., Sapoznik, K.A., Warner, R.L., and Gast, T.J. (2019). Adaptive optics imaging of the human retina. Prog. Retin. Eye Res. *68*, 1–30. https://doi.org/10.1016/j.preteyeres.2018.08.002.

27. Jung, H., Liu, J., Liu, T., George, A., Smelkinson, M.G., Cohen, S., Sharma, R., Schwartz, O., Maminishkis, A., Bharti, K., et al. (2019). Longitudinal adaptive optics fluorescence microscopy reveals cellular mosaicism in patients. JCI Insight *4*, e124904. https://doi.org/10.1172/jci.insight.124904.

28. Tam, J., Liu, J., Dubra, A., and Fariss, R. (2016). *In vivo* imaging of the human retinal pigment epithelial mosaic using adaptive optics enhanced indocyanine green ophthalmoscopy. Invest. Ophthalmol. Vis. Sci. *57*, 4376–4384. https://doi.org/10.1167/iovs.16-19503.

29. Dubra, A., and Sulai, Y. (2011). Reflective afocal broadband adaptive optics scanning ophthalmoscope. Biomed. Opt. Express *2*, 1757–1768. https://doi.org/10.1364/BOE.2.001757.

30. Flower, R.W., Fryczkowski, A.W., and McLeod, D.S. (1995). Variability in choriocapillaris blood flow distribution. Invest. Ophthalmol. Vis. Sci. *36*, 1247–1258.

31. Fryczkowski, A.W. (1994). Anatomical and functional choroidal lobuli. Int. Ophthalmol. *18*, 131–141. https://doi.org/10.1007/BF00915961.

32. Kiryu, J., Shahidi, M., Mori, M.T., Ogura, Y., Asrani, S., and Zeimer, R. (1994). Noninvasive visualization of the choriocapillaris and its dynamic filling. Invest. Ophthalmol. Vis. Sci. *35*, 3724–3731.

33. Torczynski, E., and Tso, M.O. (1976). The architecture of the choriocapillaris at the posterior pole. Am. J. Ophthalmol. *81*, 428–440. https://doi.org/10.1016/0002-9394(76)90298-1.

34. Gambaruto, A.M. (2015). Computational haemodynamics of small vessels using the Moving Particle Semi-implicit (MPS) method. J. Comput. Phys. *302*, 68–96. https://doi.org/10.1016/j.jcp.2015.08.039.

35. Gambaruto, A.M. (2015). Simulation of Red Blood Cells in a Retina Capillary. https://youtu.be/beY2z2IcZ6g.

36. Hudetz, A.G. (1997). Blood flow in the cerebral capillary network: a review emphasizing observations with intravital microscopy. Microcirculation *4*, 233–252. https://doi.org/10.3109/10739689709146787.

37. Garnier, M., Attali, J.R., Valensi, P., Delatour-Hanss, E., Gaudey, F., and Koutsouris, D. (1990). Erythrocyte deformability in diabetes and erythrocyte membrane lipid composition. Metabolism *39*, 794–798. https://doi.org/10.1016/0026-0495(90)90121-R.

38. Murakawa, K., Kohno, M., Yasunari, K., Yokokawa, K., Kurihara, N., Nagasawa, T., Kinoshita, Y., and Takeda, T. (1989). Effect of salt-loading on erythrocyte deformability in spontaneously hypertensive and Wistar-Kyoto rats. Life Sci. *45*, 1089–1095. https://doi.org/10.1016/0024-3205(89)90166-5.

39. Tillmann, W., Levin, C., Prindull, G., and Schröter, W. (1980). Rheological properties of young and aged human erythrocytes. Klin. Wochenschr. *58*, 569–574. https://doi.org/10.1007/BF01477168.

40. Başkurt, O., Levi, E., Andaç, S., and Çağlayan, S. (1990). Effect of sulfur dioxide inhalation on erythrocyte deformability. Clin. Hemorheol. Microcirc. *10*, 485–489. https://doi.org/10.3233/CH-1990-10504.

41. Hamidi, M., Zarrin, A., Foroozesh, M., and Mohammadi-Samani, S. (2007). Applications of carrier erythrocytes in delivery of biopharmaceuticals. J. Control Release *118*, 145–160. https://doi.org/10.1016/j.jconrel.2006.06.032.

42. Ahmad, S.S., Tanveer, Y., Siddique, M., and Saleem, Z. (2020). Controversies in the association of parapapillary atrophy with glaucoma. Taiwan J. Ophthalmol. *10*, 243–249. https://doi.org/10.4103/tjo.tjo_64_19.

43. Kubota, T., Jonas, J.B., and Naumann, G.O. (1993). Direct clinico-histological correlation of parapapillary chorioretinal atrophy. Br. J. Ophthalmol. *77*, 103–106. https://doi.org/10.1136/bjo.77.2.103.

44. Alm, A., and Bill, A. (1973). Ocular and optic nerve blood flow at normal and increased intraocular pressures in monkeys (Macaca irus): a study with radioactively labelled microspheres including flow determinations in brain and some other tissues. Exp. Eye Res. *15*, 15–29. https://doi.org/10.1016/0014-4835(73)90185-1.

45. Cao, J., McLeod, S., Merges, C.A., and Lutty, G.A. (1998). Choriocapillaris degeneration and related pathologic changes in human diabetic eyes. Arch. Ophthalmol. *116*, 589–597. https://doi.org/10.1001/archopht.116.5.589.

46. Lutty, G., Grunwald, J., Majji, A.B., Uyama, M., and Yoneya, S. (1999). Changes in choriocapillaris and retinal pigment epithelium in age-related macular degeneration. Mol. Vis. *5*, 35.

47. Farkas, E., and Luiten, P.G. (2001). Cerebral microvascular pathology in aging and Alzheimer's disease. Prog. Neurobiol. *64*, 575–611. https://doi.org/10.1016/S0301-0082(00)00068-X.

48. Abramoff, M.D., Magalhães, P.J., and Ram, S.J. (2004). Image processing with ImageJ. Biophotonics Int. *11*, 36–42.

49. Prum, B.E., Jr., Lim, M.C., Mansberger, S.L., Stein, J.D., Moroi, S.E., Gedde, S.J., Herndon, L.W., Jr., Rosenberg, L.F., and Williams, R.D. (2016). Primary open-angle glaucoma suspect preferred practice pattern(®) guidelines. Ophthalmology *123*, P112–P151. https://doi.org/10.1016/j.ophtha.2015.10.055.

50. Gedde, S.J., Vinod, K., Wright, M.M., Muir, K.W., Lind, J.T., Chen, P.P., Li, T., and Mansberger, S.L.; American Academy of Ophthalmology Preferred Practice Pattern Glaucoma Panel (2021). Primary open-angle glaucoma preferred practice pattern®. Ophthalmology *128*, 71–150.

51. Scoles, D., Sulai, Y.N., Langlo, C.S., Fishman, G.A., Curcio, C.A., Carroll, J., and Dubra, A. (2014). *In vivo* imaging of human cone photoreceptor inner segments. Invest. Ophthalmol. Vis. Sci. *55*, 4244–4251. https://doi.org/10.1167/iovs.14-14542.

52. Lu, R., Aguilera, N., Liu, T., Liu, J., Giannini, J.P., Li, J., Bower, A.J., Dubra, A., and Tam, J. (2021). *In-vivo* sub-diffraction adaptive optics imaging of photoreceptors in the human eye with annular pupil illumination and sub-Airy detection. Optica *8*, 333–343. https://doi.org/10.1364/OPTICA.414206.

53. Rossi, E.A., Rangel-Fonseca, P., Parkins, K., Fischer, W., Latchney, L.R., Folwell, M.A., Williams, D.R., Dubra, A., and Chung, M.M. (2013). *In vivo* imaging of retinal pigment epithelium cells in age related macular degeneration. Biomed. Opt. Express *4*, 2527–2539. https://doi.org/10.1364/boe.4.002527.

54. Tracey, B.M., Mayo, L.N., Le, C.T., Chen, V.Y., Weichsel, J., Renner, C.Y., Li, J., Tsai, J.J., Kalarn, S.P., Ou, M.T., et al. (2019). Measurement of retinal microvascular blood velocity using erythrocyte mediated velocimetry. Sci. Rep. *9*, 20178. https://doi.org/10.1038/s41598-019-56239-8.

55. Wang, D., Haytham, A., Mayo, L., Tao, Y., and Saeedi, O. (2019). Automated retinal microvascular velocimetry based on

erythrocyte mediated angiography. Biomed. Opt. Express *10*, 3681–3697. https://doi.org/10.1364/BOE.10.003681.

56. Dubra, A., and Harvey, Z. (2010). Registration of 2D Images from Fast Scanning Ophthalmic Instruments (Springer Berlin Heidelberg), pp. 60–71.

57. Donnelly, W.J., and Roorda, A. (2003). Optimal pupil size in the human eye for axial resolution. J. Opt. Soc. Am. Opt. Image Sci. Vis. *20*, 2010–2015. https://doi.org/10.1364/JOSAA.20.002010.

58. Tam, J., Martin, J.A., and Roorda, A. (2010). Noninvasive visualization and analysis of parafoveal capillaries in humans. Invest. Ophthalmol. Vis. Sci. *51*, 1691–1698. https://doi.org/10.1167/iovs.09-4483.

59. Frangi, A.F., Niessen, W.J., Vincken, K.L., and Viergever, M.A. (1998). Multiscale Vessel Enhancement Filtering (Springer Berlin Heidelberg), pp. 130–137.

60. Falk, T., Mai, D., Bensch, R., Çiçek, Ö., Abdulkadir, A., Marrakchi, Y., Böhm, A., Deubner, J., Jäckel, Z., Seiwald, K., et al. (2019). U-Net: deep learning for cell counting, detection, and morphometry. Nat. Methods *16*, 67–70. https://doi.org/10.1038/s41592-018-0261-2.

61. Ronneberger, O., Fischer, P., and Brox, T. (2015). U-net: Convolutional Networks for Biomedical Image Segmentation (Springer International Publishing), pp. 234–241.

62. Munkres, J. (1957). Algorithms for the assignment and transportation problems. J. Soc. Ind. Appl. Math. *5*, 32–38.

STAR★METHODS

KEY RESOURCES TABLE

REAGENT or RESOURCE	SOURCE	IDENTIFIER
Experimental models: Organisms/strains		
male rhesus monkeys (*Macaca mulatta*)	Harlan Laboratories and Rhenos LLC, Buckshire Corp.	HS0804005, 11 years old (Harlan) 0205047, 17 years old (Rhenos LLC)
Software and algorithms		
MATLAB	Mathworks	https://www.mathworks.com/products/matlab.html
ImageJ	Abramoff et al.[48]	https://imagej.nih.gov/ij/
Python	PyTorch	https://www.python.org/
Other		
Spectralis HRA+OCT	Heidelberg Engineering GmbH	https://www.heidelbergengineering.com/us/company/

RESOURCE AVAILABILITY

Lead contact

Further information and requests for resources should be directed to and will be fulfilled by the lead contact, Dr. Osamah Saeedi (OSaeedi@som.umaryland.edu).

Materials availability

This study did not generate new unique reagents.

Data and code availability

- Data underlying the findings of this study are available from the lead contact upon reasonable request.
- Custom codes which have not been previously described in the published literature used in this research are available from the lead contact upon reasonable request.
- Any additional information required to reanalyze the data reported in this paper is available from the lead contact upon reasonable request.

EXPERIMENTAL MODEL AND SUBJECT DETAILS

Non-human primates

Two healthy male rhesus monkeys (*Macaca mulatta*, 11 and 17 years old, additional details in key resources table) were used for this study. Each NHP underwent several imaging sessions under general anesthesia with paralysis to control for eye movements (imaging and anesthesia protocol included in method details below). Both eyes from each animal were imaged during each session. Baseline optical coherence tomography (OCT) scans were taken during imaging sessions to assess and monitor ocular health over time. This study adhered to the protocol approved by the Institutional Animal Care and Use Committee at the University of Maryland, Baltimore. Data from all four eyes of two NHPs imaged were included for qualitative assessment of erythrocyte stasis.

Human subjects

Human subjects for this study were recruited from the Department of Ophthalmology and Visual Sciences at the University of Maryland, Baltimore (additional details in Table S1). Control subjects were recruited from the optometry practice and glaucoma or glaucoma suspect subjects from the glaucoma practice. This study was approved by the institutional review boards of the University of Maryland, Baltimore and the National Institutes of Health (NIH) and was conducted in accordance with the Declaration of Helsinki. Informed consent was obtained from all participants prior to enrollment. To be eligible for inclusion,

subjects had to be at least 18 years of age, have open angles on gonioscopy, best corrected visual acuity of at least 20/200 in the study eye, and be designated control, glaucoma, or glaucoma suspect. The diagnosis of glaucoma suspect includes subjects who have characteristics of glaucoma that may suggest early disease but do not fit the diagnostic criteria of the disease, such as those with elevated intraocular pressure but no detectable structural and functional loss based on OCT or perimetry. Subjects were excluded from participation if they had a known allergy to ICG, iodine, or shellfish, were pregnant or nursing, had significant liver disease or uremia, or were participating in any other investigational drug study.

All subjects received detailed ophthalmic examination by an experienced glaucoma specialist (OJS) who then assigned the diagnosis of glaucoma, glaucoma suspect, or control based on the preferred practice patterns of the American Academy of Ophthalmology.[49,50] Controls had normal appearing optic nerves with cup to disc ratio of 0.4 or less, normal retinal nerve fiber layer thickness, and intraocular pressure less than 21 at all visits. There were no significant differences in the number of subjects with diabetes and hypertension between groups. A subset of two enrolled subjects were recruited for AO-EMA imaging (described below), which took place at the National Eye Institute (NEI) at the NIH in Bethesda, Maryland. For these subjects, an additional informed consent was obtained for the procedures performed at the NEI. These additional procedures were performed over multiple visits: baseline imaging two weeks prior to EMA to verify the absence of any ICG signal, AO-EMA imaging the same day as EMA imaging at the University of Maryland (2–3 hours after injection to account for travel time), and follow up imaging one day and two weeks after the initial AO-EMA imaging. In one subject, AO-EMA was repeated one year afterwards.

In total, 37 eyes of 22 human subjects underwent EMA imaging. Depending on the ability of the subject to complete the imaging procedures and the resulting image quality, images from a subset of patients were used for each analysis (Table S1). For quantification of erythrocyte stasis in the FAZ, 31 eyes of 18 subjects were analyzed: six eyes of four human subjects were excluded as they did not have OCTA that could be used to accurately identify the FAZ (OCTA instrumentation was acquired 2 years into the study). For the analysis on determining the distribution of erythrocyte stasis, 21 eyes of 16 subjects were analyzed: 12 eyes of 12 subjects had macular angiograms but did not have peripapillary angiogram, two eyes of one patient had no peripapillary or macula angiograms, and two eyes of two subjects were excluded due to excessive motion artifact or variability, making image registration and analysis impossible. As mentioned above, two subjects were co-enrolled in a study of AO and in-depth analysis was completed on images of those four eyes.

EMA preparation

The same process for labeling erythrocytes was followed for both NHPs and humans, based on previously published procedures.[18] Briefly, 17 mL of blood was drawn prior to imaging, on the day of the procedure. Erythrocytes were isolated from whole blood in a sterile fashion, loaded with ICG and prepared for autologous injection. Up to 1 mL of autologous ICG-loaded erythrocytes were injected intravenously in NHPs, and up to 4 mL of autologous ICG-loaded erythrocytes were intravenously injected into human subjects. NHP preparation and injections took place at the University of Maryland School of Medicine, and human erythrocyte preparation and injections took place in the General Clinical Research Center within the University of Maryland Medical Center. The physical configuration of the ICG-loaded erythrocytes was checked under the microscope prior to injection.[17]

METHOD DETAILS

NHP imaging

Prior to injection, the NHPs were anesthetized with ketamine (5–10 mg/kg) and xylazine (0.2–0.4 mg/kg), and paralyzed with vecuronium (40–60 μg/kg, followed by 0.35–45 μg/kg/min). NHPs were intubated with an endotracheal tube and given 100% oxygen from an isoflurane anesthesia unit. A thermal blanket was used to maintain body temperature throughout the session. NHPs were dilated with Tropicamide 1% and a wire lid speculum was used to separate the lids of the eye being examined. While lying in the prone position, averaged 15, 20, and 30-degree field of view (FOV) images centered on the macula were obtained using the Automatic Real-time Tracking (ART) Mean function of a Heidelberg Retinal Angiograph + Optical Coherence Tomography (HRA + OCT) device (Heidelberg Engineering GmbH, Germany). Optical coherence tomography angiography (OCTA) was performed at the macula using the same device. Balanced salt solution was used throughout the imaging session to lubricate the cornea. NHP heart rate, blood pressure, body temperature, respiratory rate, oxygen saturation (SpO_2), and end tidal carbon

dioxide levels were monitored throughout the imaging session. A topical antibiotic ointment (erythromycin) was applied to the eyelids at the end of each imaging session to prevent ocular infection.

Standard EMA in human

The patients' heart rate, respiratory rate, blood pressure, and temperature were monitored at baseline and recorded throughout the session. Prior to erythrocyte injection, human participants underwent pupillary dilation using Tropicamide 1% at the University of Maryland Medical Center. Retinal angiograms were obtained using an SLO (Heidelberg Retinal Angiograph 2, Heidelberg Engineering GmbH, Germany). Angiograms were taken at the peripapillary and macular regions of each study eye using a 15-degree horizontal by 7.5-degree vertical FOV at a rate of 24.6 frames per second centered at the optic disc or fovea respectively. Averaged 30-degree FOV Automated Real-time Tracking (ART) images of the retina were also obtained. OCTA was performed, centered on the macula.

AO-EMA

Prior to imaging, eyes of each subject were dilated with Tropicamide 1% at the NEI. Multimodal AO-SLO imaging was performed[27] using a custom-built instrument that incorporates confocal reflectance,[29] non-confocal split detection,[51] and AO-ICG.[28] These three imaging channels were used primarily to visualize reflective cone photoreceptors, inner retinal vasculature, and choriocapillaris/ICG-loaded erythrocytes, respectively. Briefly, the system uses a 790 nm superluminescent diode (SLD) (S-790-G-I-15-M, Superlum, Ireland) for imaging and an 880 nm SLD (SLD-mCS-341-HP1-SM-880, Superlum, Ireland) for wavefront sensing. AO-ICG imaging was performed with a 5 Airy Disk Diameter pinhole, expected to provide an axial resolution of ~35 μm.[52] For each eye, a total of 40 to 80 videos, each 20-seconds to 2-minutes long (16.7 frames per second), were acquired at various locations near the macula. During image acquisition, the subject was asked to look at a computer-controlled fixation target[53] and to blink naturally.

At all visits, subjects were imaged across a 30° FOV using a commercially available SLO capable of detecting ICG to identify locations of any erythrocytes in stasis (Spectralis HRA+OCT, Heidelberg Engineering GmbH, Germany). At the baseline visit, SLO and AO images were used to confirm the absence of erythrocytes in stasis. On the day of EMA imaging, AO-SLO imaging was performed immediately after SLO imaging at locations of identified cells in stasis (square FOV ranging from 1 to 2° on the retina). At selected stasis locations, a series of AO images was sequentially acquired at different focal planes. SLO imaging was repeated every hour in between AO-SLO imaging acquisitions to track the dynamics of erythrocytes in stasis, over a total of three to four hours, which included frequent breaks throughout imaging. A follow up visit was performed one day later to confirm the presence or absence of ICG-loaded erythrocytes in stasis. At the final visit two weeks post EMA injection, SLO imaging was repeated and then AO-ICG angiography was performed to map out the choriocapillaris following intravenous administration of 25 mg of ICG dye dissolved in 3 mL of aqueous solution.[10]

Data processing and analysis

Preprocessing

For standard EMA, angiograms collected during the human imaging sessions were registered to minimize the effects of eye movement and contrasted to optimize detection of cells in stasis using a custom MATLAB (MathWorks, vR2019a) script.[54,55]

For AO-EMA, eye motion was corrected following standard procedures,[56] and averaged AO images were assembled into a larger montage and registered to the SLO images for comparison.

Erythrocyte stasis in the FAZ (standard EMA)

To identify erythrocytes in stasis in the choroidal circulation, stationary cells located within the FAZ in NHPs and humans were counted. Temporally averaged EMA images of at least 25 sequential frames were used to identify cells in stasis. *En face* OCTA images were superimposed onto the averaged EMA image, permitting delineation of the FAZ border, a region devoid of retinal vasculature. The number of cells in stasis within the FAZ were counted.

Distribution of stasis events (standard EMA)

For each angiogram, we used the temporal average (TA) of 25 consecutive EMA frames to visualize erythrocytes in stasis for at least one second. This resulted in 5 to 15 images per video which were analyzed to

assess the distribution of erythrocytes in stasis across different retinal locations. Erythrocytes in stasis in the peripapillary and macular regions were identified using a validated neural network as described in more details below (see "dataset annotation").

The number and distribution of the cell densities in the disc and macula regions for control and glaucoma subjects were subsequently analyzed. In this analysis glaucoma and glaucoma suspect subjects were grouped together and compared to the control group. The absolute number of cells in the macula and the peripapillary area were compared between these two groups as well as the relative number (to account for alterations in concentrations of labeled erythrocytes), which was characterized using the ratio of cells in the peripapillary area to the macular area (peripapillary to macular ratio, PMR). A generalized estimating equation was used to account for using two eyes of the same subject.

Axial localization of erythrocyte stasis (AO-EMA)

Since the AO-SLO system uses a larger imaging beam compared to the SLO, the AO-SLO system had a higher axial resolution[57] than the SLO system used in this study. This allowed for better axial localization of each ICG-labeled cell in stasis, based on the calculation of FWHM values of the ICG signal profile of each cell across the different focal planes, ranging from inner retinal layer to near the choroid (FWHM values were expected to be the smallest when the cell is in focus and to be larger when the cell is out of focus). The corresponding confocal reflectance and split detection images were used to determine the axial location of the focal planes. Retinal vessels were visible in the split detection channel when the focal plane was set near the inner retina, and the cone photoreceptors were visible in the confocal reflectance channel when the focal plane was set near both the photoreceptor and choriocapillaris layers.[10] To evaluate changes in FWHM measurements across different AO focal planes, the choriocapillaris focal plane was set as the origin, and focal shifts were converted from diopters to millimeters based on a modified Bennett-Rabbett model eye in which the axial length, corneal curvature, and anterior chamber depth measurements (IOL Master, Zeiss) from the subject's dilated eye were used.

Mapping the choriocapillaris and FAZ (AO-EMA)

In vivo images of the choriocapillaris were obtained by imaging ICG dye using AO-SLO.[10] Briefly, the ICG fluorescent signal profile over time was measured over the initial two minutes of the transit phase after a bolus of ICG dye was delivered intravenously. As expected, multiple fluorescent peaks were identified, corresponding to the initial passage of dye through the eye and subsequent recirculation of dye. Choriocapillaris images were obtained by subtracting the averaged ICG signal after dye recirculation (one to two minutes after injection) from the averaged ICG signal during the passage of the initial bolus (10 to 20 seconds after injection). Up to two choriocapillaris images could be obtained per subject by splitting the total 3 mL ICG dose into two sequentially-administered doses of 1 and 2 mL ICG. Simultaneously-acquired images of the cone photoreceptors were used to co-register images of the choriocapillaris with other AO images.

Images of the parafoveal retinal capillaries were obtained from non-confocal split detection AO videos acquired with the focal plane set to the inner retina. The vascular structure was calculated based on motion contrast enhancement.[23,58] Briefly, for each video, a pixel-by-pixel standard deviation image was calculated on an eye-motion corrected video. Some pixels at the edges of each image were not visible due to eye motion that shifted the location of the retina being imaged from frame to frame. Therefore, the standard deviation calculation was performed on a subset of available pixels. The resulting images of perfused retinal vessels were montaged to map the FAZ. Similar to above, simultaneously acquired confocal reflectance images of photoreceptors were used to co-register images of the parafoveal capillaries with other AO images.

AO-ICG choriocapillaris segmentation

Segmentation of choriocapillaris was performed as described previously.[10] First, Hessian-based Frangi filter[59] was applied to the AO-ICG choriocapillaris image using MATLAB (MathWorks, vR2021a), which resulted a binary mask of vessel segments. Next, manual correction was performed by overlaying the binary mask on top of the choriocapillaris image to correct for any errors in segmentation (Figure S2). To compare locations of cells in stasis from multiple EMA procedures, images were spatially registered to the binarized choriocapillaris map based on retinal landmarks. All observed cells in stasis were then marked and categorized according to imaging modalities and time points.

The probability that cells in stasis were localized to choriocapillaris vessel segments was assessed using a one-sided binomial test, with the expected probability of success set to be the percentage of pixels corresponding to choriocapillaris vessel lumens across the image (68%).

Automated detection of erythrocyte stasis using deep learning

Dataset annotation. For each eye, four scanning laser ophthalmoscope (SLO) images were selected with two 15-by-7.5-degree ROIs centered at the optic nerve head (excluding the optic nerve head itself), and two 15-by-7.5-degree ROIs centered on the macular region (Figures 5A and 5B). If there was overlap between the optic nerve head and macula ROIs, then the macula ROI was further cropped to exclude the area of overlap. Two expert graders manually identified erythrocytes in stasis in a total of 24 images from which binary masks were generated using pixel by pixel labeling. Inconsistent labels from the two graders were arbitrated by a third expert grader to achieve a final set of consensus annotations.

Network architecture, training, evaluation. The erythrocyte detection network was implemented in PyTorch using a regression-based neural network[60] as shown in Figure S3. The network design followed the U-net architecture[61] except that a regression map generated by the distance transformation of the ground truth binary mask was used for training. Compared to the binary mask, the distance map preserved the erythrocyte spatial information, while at the same time, it reinforced the prediction importance for the cell centroid positions while weakening the prediction importance for cell boundaries. During training, data augmentation was carried out in a patch-based manner, in which 48 by 48-pixel randomly cropped image patches were augmented following random transformations (rotation, mirroring, and translation). The network parameters were optimized using the Adam algorithm with an initial learning rate of 3×10^{-4}, betas = (0.9, 0.999).

Following training, the cell detection model was applied to full-sized SLO images using sliding windows with a step size of 16 pixels in both horizontal and vertical directions. The outputs from all sliding windows were merged to reconstruct the distance map prediction over the full-sized SLO image. Erythrocyte locations were determined as the local maximum of the distance map constructed using a 5 by 5 set of neighboring pixels. An example of detected cells is shown in Figures S3B and S3C.

Evaluation was performed using a six-fold cross validation strategy (leave-one-eye). Specifically, in each cross-validation folder, 20 images from five eyes (four images per eye) were used for network training and four images from the remaining eye were used for network validation. The predicted cells were matched with ground truth cells according to a linear assignment Kuhn-Munkres algorithm[62] based on the Cartesian distance cost function. Overall, the automated cell detection algorithm achieved favorable detection accuracy, with an average F1 score of 93.8±2.8% (mean±SD) across the six folds (Table S2). Although there were some incorrect predictions, the overall cell count predictions across the complete dataset were highly correlated with the ground truth cell counts (R^2 = 0.9827, $p<0.001$; Figure S3D). The average relative counting error (ratio between absolute count error and total cell counts) was 1.27%. These results demonstrate the performance of the regression-based U-net model for automated detection of erythrocytes on EMA images.

QUANTIFICATION AND STATISTICAL ANALYSIS

Data are represented as mean ± standard deviation (SD). The exact values of n are indicated. A binomial test was used to calculate the likelihood that all cells observed in stasis across different visits were located within the choriocapillaris lumens (see section "correlative multimodal imaging of erythrocyte stasis reveals localization to the choroidal microvasculature"). Generalized estimating equation was used to compare the difference in the relative distribution of cells in stasis between control and glaucoma eyes (Figure 5). All tests were conducted using Matlab or Python. Statistical significance was set at $p < 0.05$.